

See discussions, stats, and author profiles for this publication at: <https://www.researchgate.net/publication/242652090>

# Surface Functionalization of Nanostructured Fe<sub>2</sub>O<sub>3</sub> Polymorphs: From Design to Light-Activated Applications

ARTICLE in ACS APPLIED MATERIALS & INTERFACES · JUNE 2013

Impact Factor: 6.72 · DOI: 10.1021/am401475g · Source: PubMed

CITATIONS

13

READS

100

13 AUTHORS, INCLUDING:



[Giorgio Carraro](#)

University of Padova

72 PUBLICATIONS 434 CITATIONS

[SEE PROFILE](#)



[Alberto Gasparotto](#)

University of Padova

255 PUBLICATIONS 2,961 CITATIONS

[SEE PROFILE](#)



[Chitta Das](#)

Brandenburg University of Technology Cottbu...

7 PUBLICATIONS 48 CITATIONS

[SEE PROFILE](#)



[Urska Lavrencic Stangar](#)

University of Nova Gorica

4 PUBLICATIONS 79 CITATIONS

[SEE PROFILE](#)

# Surface Functionalization of Nanostructured Fe<sub>2</sub>O<sub>3</sub> Polymorphs: From Design to Light-Activated Applications

Davide Barreca,<sup>†</sup> Giorgio Carraro,<sup>‡</sup> Alberto Gasparotto,<sup>‡</sup> Chiara Maccato,<sup>\*,‡</sup> Francesca Rossi,<sup>§</sup> Giancarlo Salvati,<sup>§</sup> Massimo Tallarida,<sup>⊥</sup> Chittaranjan Das,<sup>⊥</sup> Fernando Fresno,<sup>#</sup> Dorota Korte,<sup>#</sup> Urška Lavrenčič Stangar,<sup>#</sup> Mladen Franko,<sup>#</sup> and Dieter Schmeisser<sup>⊥</sup>

<sup>†</sup>IENI-CNR and INSTM, Department of Chemistry, Padova University, Via Marzolo 1, 35131 Padova, Italy

<sup>‡</sup>Department of Chemistry, Padova University and INSTM, Via Marzolo 1, 35131 Padova, Italy

<sup>§</sup>IMEM-CNR, Parco Area delle Scienze 37/A, 43124 Parma, Italy

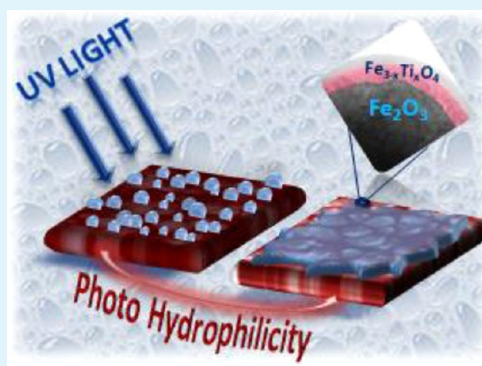
<sup>⊥</sup>Brandenburg University of Technology, Konrad Wachsmann Allee 17, 03046 Cottbus, Germany

<sup>#</sup>Laboratory for Environmental Research, Nova Gorica University, Vipavska 13, 5001 Nova Gorica, Slovenia

## S Supporting Information

**ABSTRACT:** Nanostructured iron(III) oxide deposits are grown by chemical vapor deposition (CVD) at 400–500 °C on Si(100) substrates from Fe(hfa)<sub>2</sub>TMEDA (hfa = 1,1,1,5,5,5-hexafluoro-2,4-pentanedionate; TMEDA = N,N,N',N'-tetramethylethylenediamine), yielding the selective formation of  $\alpha$ -Fe<sub>2</sub>O<sub>3</sub> or the scarcely studied  $\epsilon$ -Fe<sub>2</sub>O<sub>3</sub> polymorphs under suitably optimized preparative conditions. By using Ti(OPr<sup>i</sup>)<sub>4</sub> (OPr<sup>i</sup> = iso-propoxy) and water as atomic layer deposition (ALD) precursors, we subsequently functionalized the obtained materials at moderate temperatures (<300 °C) by an ultrathin titanomagnetite (Fe<sub>3–x</sub>Ti<sub>x</sub>O<sub>4</sub>) overlayer. An extensive multitechnique characterization, aimed at elucidating the system structure, morphology, composition and optical properties, evidenced that the photoactivated hydrophilic and photocatalytic behavior of the synthesized materials is dependent both on iron oxide phase composition and ALD surface modification. The proposed CVD/ALD hybrid synthetic approach candidates itself as a powerful tool for a variety of applications where semiconductor-based nanoarchitectures can benefit from the coupling with an ad hoc surface layer.

**KEYWORDS:** chemical vapor deposition, atomic layer deposition, iron oxide, titanomagnetite, photoactivated properties



## INTRODUCTION

Iron(III) oxide has recently attracted a great deal of attention for its promising light-activated functional properties, coupled with its large abundance and low toxicity.<sup>1,2</sup> In particular,  $\alpha$ -Fe<sub>2</sub>O<sub>3</sub> (hematite,  $E_g = 2.1$  eV), the most thermodynamically stable Fe<sub>2</sub>O<sub>3</sub> polymorph, has emerged as an efficient photocatalyst for solar hydrogen production<sup>3–5</sup> and as a promising electrode material for dye-sensitized solar cells.<sup>2,6–8</sup> Nevertheless, in spite of the inherent hematite technological potential, its performances in light-assisted applications are hindered by the relatively low absorption coefficient, poor charge carrier mobility and reduced electron/hole (e<sup>–</sup>/h<sup>+</sup>) lifetime.<sup>9–11</sup> Interestingly, such drawbacks can be partially overcome by nanostructuring iron oxide to enable an efficient light harvesting and minimize carrier diffusion distances, suppressing thus detrimental recombination losses.<sup>2,6,7,12–14</sup> To achieve such goals, a promising alternative strategy consists of iron oxide functionalization by a suitable ultrathin surface layer. Beside passivating Fe<sub>2</sub>O<sub>3</sub> surface trap states, the precise engineering of the resulting heterointerface provides in fact further degrees of freedom to tailor light absorption and charge carrier transport phenomena.<sup>6,14,15</sup> In

addition, the growth of an ad hoc surface layer is also expected to offer improved corrosion protection to the underlying iron oxide matrix, an important issue in view of practical applications.<sup>16</sup>

The high potential of surface modification in attaining improved material performances has been recently demonstrated for  $\alpha$ -Fe<sub>2</sub>O<sub>3</sub> and other semiconducting oxides such as TiO<sub>2</sub> and Cu<sub>2</sub>O, coated by an ultrathin layer of Al<sub>2</sub>O<sub>3</sub>, MgO, SiO<sub>2</sub>, and other oxides.<sup>6,16–18</sup> Notwithstanding the general applicability of this approach, its exploitation relies on the precise control of the surface overlayer features that, in turn, depend on the adopted synthetic technique. In this context, ALD has been proved to possess superior properties with respect to other preparation routes because of its repeatability, perfect conformality and nanometer-scale thickness control at low deposition temperatures.<sup>14,19–21</sup> In particular, the latter feature is of great importance to ensure surface functionalization of the target matrix preventing, at the same time, undesired morphological alterations.

**Received:** April 22, 2013

**Accepted:** June 27, 2013

Recently, Kronawitter et al. have reported on the ALD of an ultrathin  $\text{Ti}_x\text{O}_y$  layer on  $\alpha\text{-Fe}_2\text{O}_3$ ,<sup>22</sup> evidencing the occurrence of a remarkable structural and electronic interplay at the  $\text{Ti}_x\text{O}_y/\text{Fe}_2\text{O}_3$  interface. Such materials have been recently proposed for applications in various technological fields, from water photoelectrolysis to gas sensing and dye-sensitized solar cells.<sup>13,18,23,24</sup> Starting from these results and basing on our recent studies on the selective CVD growth of various  $\text{Fe}_2\text{O}_3$  polymorphs,<sup>1,25,26</sup> in the present work we report on the unique features of a combined CVD/ALD strategy for the fabrication of surface-functionalized  $\alpha$ - and  $\epsilon\text{-Fe}_2\text{O}_3$  nanodeposits with tailored properties. In particular, our attention is focused on the photoinduced hydrophilicity (PH) and photocatalytic (PC) activity of such systems in view of antifogging and self-cleaning applications. Though these two processes are based on different phenomena,<sup>27</sup> their common feature is the photoassisted generation of  $e^-/h^+$  pairs, whose subsequent fate significantly affects the overall material performances. As a consequence, a detailed study of the ALD layer role on the system behavior, and of its interplay with the synthesis conditions, represents a key issue in understanding the properties of functionalized  $\alpha$ - and  $\epsilon\text{-Fe}_2\text{O}_3$  nanosystems. The obtained performances open intriguing perspectives for the use of combined ALD/CVD approaches in the fabrication of next-generation materials for photoassisted applications.

## EXPERIMENTAL SECTION

**Synthesis.**  $\text{Fe}(\text{hfa})_2\text{TMEDA}$  ( $\text{hfa}$  = 1,1,1,5,5,5-hexafluoro-2,4-pentanedionate; TMEDA = *N,N,N',N'*-tetramethylethylenediamine) was synthesized following a recently reported procedure<sup>25,26,28</sup> and used as CVD precursor for  $\text{Fe}_2\text{O}_3$  deposition. CVD experiments were carried out in an horizontal cold-wall reaction system equipped with an external reservoir for precursor vaporization. Depositions were performed for 60 min on HF-etched *p*-type Si(100) substrates (MEMC, Merano, Italy,  $10\text{ mm} \times 10\text{ mm} \times 1\text{ mm}$ ), subjected to a previously reported cleaning procedure.<sup>29</sup> In a typical CVD process, precursor powders (weight = 0.3 g) were heated at  $60^\circ\text{C}$  and transported toward the growth zone through gas lines maintained at  $120^\circ\text{C}$ . Water vapor was introduced in

the reaction chamber by means of an auxiliary line passing through an  $\text{H}_2\text{O}$  external reservoir kept at  $50^\circ\text{C}$ . The selective deposition of  $\alpha\text{-Fe}_2\text{O}_3$  was achieved at a growth temperature of  $500^\circ\text{C}$ , total pressure of 3.0 mbar and total  $\text{O}_2$  flow rate of 40 standard cubic centimeters per minute (sccm). For  $\epsilon\text{-Fe}_2\text{O}_3$ , the growth temperature, total pressure and total  $\text{O}_2$  flow rate were set at  $400^\circ\text{C}$ , 10.0 mbar, and 200 sccm, respectively. Hereafter, as-deposited CVD samples will be labeled as  $\alpha\text{-Fe}_2\text{O}_3$  and  $\epsilon\text{-Fe}_2\text{O}_3$ .

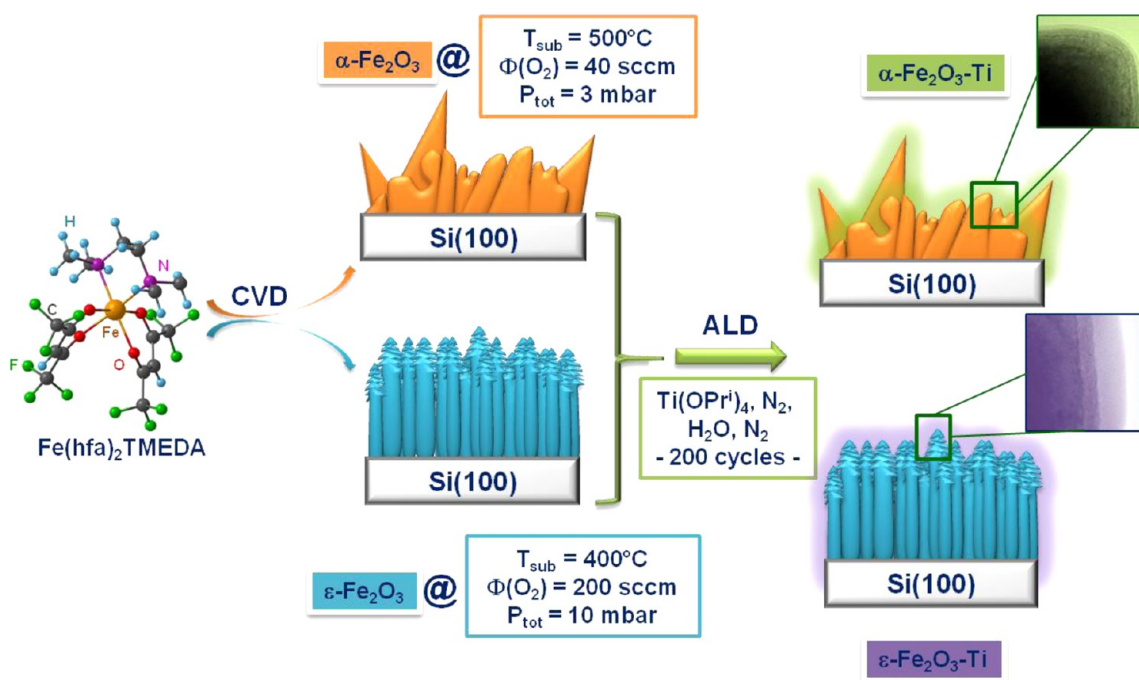
Functionalization of  $\alpha$ - and  $\epsilon\text{-Fe}_2\text{O}_3$  was performed by ALD using  $\text{Ti}(\text{OPr})_4$  ( $\text{OPr}^i$  = iso-propoxy) and water as precursors. Experiments were carried out at the Brandenburg University of Technology (BTU) in Cottbus, Germany, by a homemade ALD reactor described elsewhere.<sup>30,31</sup> After evacuating the reactor to a base pressure lower than  $1 \times 10^{-8}$  mbar, iron oxide specimens were heated to  $210^\circ\text{C}$  by a heating plate within 15 min. ALD depositions consisted of 200 cycles of the following pulsing sequence: 4 s  $\text{Ti}(\text{OPr})_4$ , 0.5 s  $\text{N}_2$  purge, 0.5 s  $\text{H}_2\text{O}$ , 0.5 s  $\text{N}_2$  purge. In the following, ALD-functionalized samples will be labeled as  $\alpha\text{-Fe}_2\text{O}_3\text{-Ti}$  and  $\epsilon\text{-Fe}_2\text{O}_3\text{-Ti}$ .

**Characterization.** High-resolution transmission electron microscopy (HR-TEM) and high angle annular dark field-scanning transmission electron microscopy (HAADF-STEM) experiments were carried out on a JEOL 2200FS field-emission microscope with in-column  $\Omega$  filter, operated at 200 kV. Specimens for plane-view and cross-sectional observations were thinned by mechanically grinding and polishing down to the thickness of approximately  $20\text{ }\mu\text{m}$ , followed by  $\text{Ar}^+$  milling up to electron transparency. Electron diffraction (ED) measurements, adopted for structural studies, have been performed over different sample regions in order to check phase homogeneity.

Field emission-scanning electron microscopy (FE-SEM) analyses were carried out by means of a Zeiss SUPRA 40VP instrument, using a primary beam acceleration voltage of 10 kV.

Synchrotron radiation photoemission spectroscopy (SR-PES) characterization was carried out at the U49/2-PGM2 beamline of the BESSY-II synchrotron radiation facility within the Helmholtz-Zentrum-Berlin. The base pressure of the photoemission chamber was of the order of  $5 \times 10^{-10}$  mbar. X-ray photons were monochromatized by a planar grating monochromator with a resolution of the order of  $\Delta E/E \approx 10^{-4}$  and focused by a refocusing mirror over a  $0.5 \times 1\text{ mm}^2$  area. Photoelectrons were detected using a Specs Phoibos 150 analyzer with an emission angle of  $45^\circ$ . For Fe2p signal acquisition, 1270 eV photons

**Scheme 1. Graphical Representation of the Synthetic Approach Developed for the CVD Growth of  $\alpha\text{-Fe}_2\text{O}_3$  and  $\epsilon\text{-Fe}_2\text{O}_3$  and Their Subsequent ALD Functionalization**





were used in order to avoid the overlap with either TiLMM or OKVV Auger features. For Ti2p peak acquisition, both 640 and 1100 eV photons were used. Binding energies were corrected for charging effects by assigning a position of 284.8 eV to the adventitious C1s photopeak.

Water contact angle (CA) experiments were performed at room temperature using a horizontal microscope with a protractor eyepiece [contact angle meter (CAM-100) from KSV Instruments, Ltd. Finland]. On each sample, measurements were repeated twice at different irradiation times to obtain average water CA values. The mean uncertainty was estimated to be ca. 8%. Zero-time angles were determined after the specimens were stored in the dark for several days. Samples were subsequently irradiated in a photochamber equipped with three UV lamps (Philips CLEO 20 W, broad maximum at 355 nm). The average incident irradiance was  $23.3 \text{ W m}^{-2}$  in the interval 300–400 nm.

PC activities were determined by monitoring the oxidation of terephthalic acid (TPA) to hydroxyterephthalic acid (HTPA), as

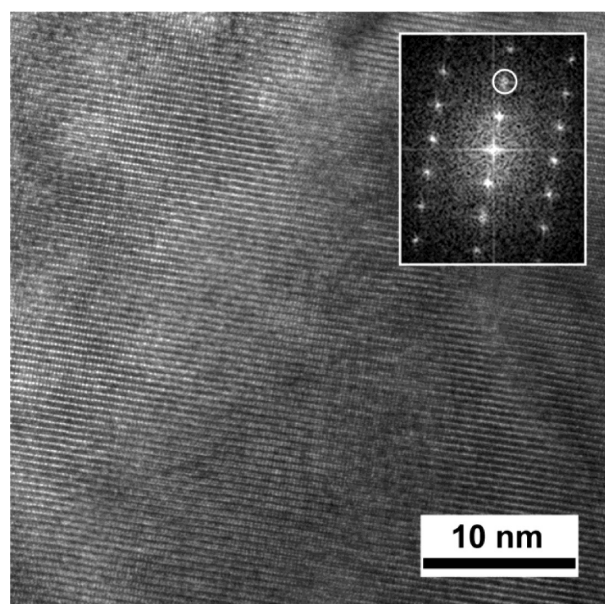


**Figure 1.** Cross-sectional HR-TEM image of the  $\alpha\text{-Fe}_2\text{O}_3$  lattice. Inset: FFT, corresponding to hematite, zone axis  $\langle 2,1,0 \rangle$ . The white circle marks the (006) spot.

previously reported.<sup>32</sup> Briefly, a TPA-containing film was deposited on the surface of each sample by dip-coating into a water/ethanol solution of sodium terephthalate and hydroxyethylcellulose. Specimens were subsequently UV-irradiated in a photochamber for fixed time intervals under the same conditions adopted for water CA tests, and finally washed with 0.25 mL of a 1:1 water/ethanol mixture per each  $\text{cm}^2$  of coated surface. HTPA concentration (average uncertainty ca.  $\pm 1 \times 10^{-8} \text{ M}$ ) was finally determined by fluorimetry in a microplate reader Tecan Infinity F200, using 320 and 430 nm as excitation and emission wavelengths, respectively. To obtain the HTPA concentration at various illumination stages, we repeated the above procedure with increasing irradiation times, with the surface of the samples washed, dried, and UV-irradiated for 30 min between consecutive measurements. For each specimen, the measured data points were then fitted according to the kinetic model described in the Results and Discussion section. The mean uncertainty on the obtained  $k_1$  values was estimated to be ca. 8%.

For photothermal beam deflection (PBD) measurements, the transverse beam deflection technique in its skimming configuration was used. Samples were illuminated by a He–Ne laser beam (MELLES GRIOT, model 25-LHP-928–230; output power = 75 mW at  $\lambda \approx 600 \text{ nm}$ ). The beam, modulated by a Vis broadband acousto-optic amplitude modulator (New Focus, model 4102-M) controlled by a high voltage amplifier (New Focus, model 3211), was directed and focused on the sample surface through an optical system (THORlabs). The generated temperature field was detected by a second, low-power (2 mW, 633 nm) He–Ne laser beam (Uniphase, Model 1103P). The intensity change of the latter was measured by a quadrant photodiode (RBM- R. Braumann GmbH, Model C30846E) connected to a lock-in amplifier (Stanford research instruments, Model SR830 DSP). All experiments were performed in air at room temperature measuring the amplitude and phase dependence of the photothermal deflection signal on the modulation frequency ( $f$ ) of the temperature field. To determine the effective (including the whole active layer) transport ( $E_a, \tau$ ) and surface ( $s, L$ ) parameters, we least-squares fitted the amplitude and phase of the experimental data as a function of  $f$  to the theoretical curves.<sup>22</sup> Further details are provided in the Supporting Information.

## RESULTS AND DISCUSSION

A sketch of the synthetic approach adopted for the fabrication of bare and functionalized iron oxide nanostructures is reported in Scheme 1.

**Structure, Morphology, and Composition.** Structural analyses on as-deposited CVD samples showed that, depending

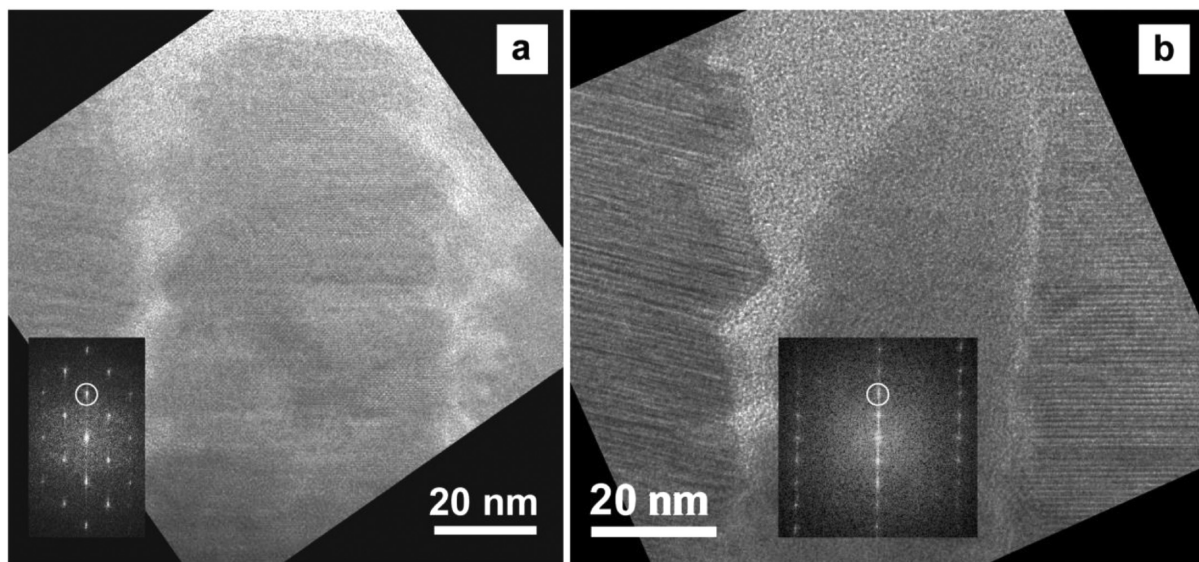


**Figure 2.** Cross-sectional HR-TEM images of  $\epsilon\text{-Fe}_2\text{O}_3$  grains. Inset in (a): FFT taken on the central grain, zone axis  $\langle 1,0,0 \rangle$ . Inset in (b): FFT taken on the right grain, zone axis  $\langle 0,1,0 \rangle$ . White circles mark the (002) spots.

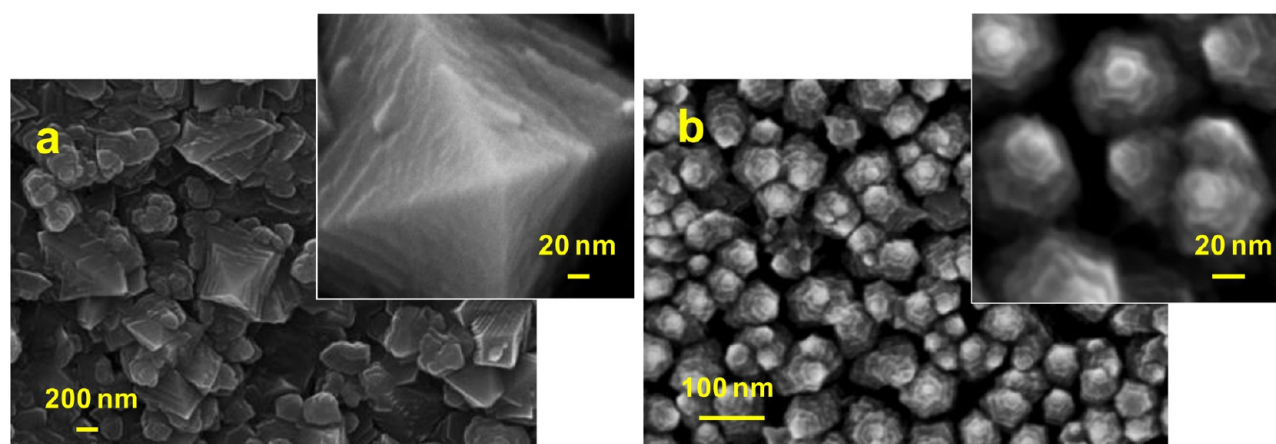


**Figure 3.** Plane-view FE-SEM micrographs for samples (a)  $\alpha$ -Fe<sub>2</sub>O<sub>3</sub>-Ti and (b)  $\epsilon$ -Fe<sub>2</sub>O<sub>3</sub>-Ti. Insets display higher-magnification images for the same specimens.

on the adopted synthesis conditions (see Experimental Section), it was possible to selectively grow either the  $\alpha$ -Fe<sub>2</sub>O<sub>3</sub> (rhombohedral, space group:  $R\bar{3}c$ ,  $a = 5.03$  Å,  $c = 13.74$  Å)<sup>33</sup> or  $\epsilon$ -Fe<sub>2</sub>O<sub>3</sub> phase (orthorhombic, space group:  $Pna2_1$ ,  $a = 5.095$  Å,  $b = 8.789$  Å,  $c = 9.437$  Å).<sup>34</sup> To this aim, Figure 1 reports a detail of a typical cross-sectional HR-TEM image, along with the corresponding fast Fourier transform (FFT), obtained on  $\alpha$ -Fe<sub>2</sub>O<sub>3</sub>. The correct symmetry and lattice parameters of the hematite structure were confirmed, and no appreciable signals pertaining to other phases were detected.

Figure 2 displays the HR-TEM images recorded in cross-section on  $\epsilon$ -Fe<sub>2</sub>O<sub>3</sub> grains. The inspection of lattice fringes and ED patterns (or FFTs as shown in the insets of Figure 2) proved the presence of  $\epsilon$ -Fe<sub>2</sub>O<sub>3</sub> as the only detectable crystalline phase. On the basis of the difficulty in stabilizing this polymorph,<sup>35</sup> we devoted particular attention to the analysis of the grain structure, but only stacking defects (see the planar stacking faults on the left and right grains in Figure 2b) without transition to other phases were detected. It is also worthwhile observing that crystalline grains were often aligned perpendicularly to the substrate surface with a  $[001]_{\epsilon} // [001]_{\text{Si}}$  preferential orientation.

The morphology of Fe<sub>2</sub>O<sub>3</sub> specimens, both before and after ALD functionalization, was investigated by FE-SEM. The bare  $\alpha$ -Fe<sub>2</sub>O<sub>3</sub> sample (see Figure S1a, b in the Supporting Information) was characterized by a bimodal distribution of pyramidal (lateral size and length = 600 and 1000 nm, respectively) and globular particles (lateral size and length = 300 and 600 nm, respectively), whose agglomeration produced a relatively disordered material topography. In a different way,  $\epsilon$ -Fe<sub>2</sub>O<sub>3</sub> (see Figure S1c, d in the Supporting Information) exhibited a more uniform morphology arising from the growth of rodlike structures perpendicular to the substrate surface. The mean nanorods lateral size and length corresponded to 80 and 350 nm, respectively, yielding an average aspect ratio (length/lateral size) > 4. It can also be observed that rods showed a cylindrical trunk ( $\approx 300$  nm) and a sharper tip ( $\approx 50$  nm). The anisotropic growth of the observed columnar structures can be associated to the  $[001]$  preferential orientation revealed by TEM analyses.

Images a and b in Figure 3 show the surface texture of  $\alpha$ -Fe<sub>2</sub>O<sub>3</sub>-Ti and  $\epsilon$ -Fe<sub>2</sub>O<sub>3</sub>-Ti, respectively. The comparison of Figure S1 in the Supporting Information with Figure 3 evidenced that the morphology of the bare Fe<sub>2</sub>O<sub>3</sub> samples did not undergo any appreciable change after ALD functionalization. This effect could be traced back to the conformal coverage capability of the

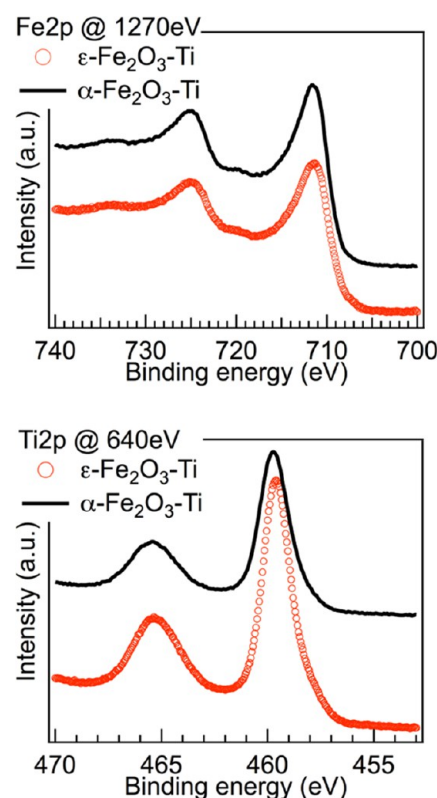


**Figure 4.** Fe2p and Ti2p SR-PES spectra of  $\alpha$ -Fe<sub>2</sub>O<sub>3</sub>-Ti (black) and  $\epsilon$ -Fe<sub>2</sub>O<sub>3</sub>-Ti (red), respectively. Both samples were measured under the same experimental conditions (electron analyzer and beamline parameters).

ALD technique<sup>19,20</sup> and to the use of relatively mild processing conditions, preventing the occurrence of thermally induced aggregation phenomena in the final systems.

To investigate the composition of the ALD layer and attempt a surface coverage estimation of the underlying iron oxide matrix, SR-PES analyses were carried out. Figure 4 displays the Fe2p and Ti2p signals for the functionalized samples.

The Fe2p line shape and positions were similar for both  $\alpha$ -Fe<sub>2</sub>O<sub>3</sub>-Ti and  $\epsilon$ -Fe<sub>2</sub>O<sub>3</sub>-Ti, and comparable with the typical photoemission spectra measured on Fe<sub>2</sub>O<sub>3</sub> samples.<sup>1,36,37</sup> The small differences between the two curves in the 707–709 eV range could be ascribed to differently coordinated Fe(III) centers



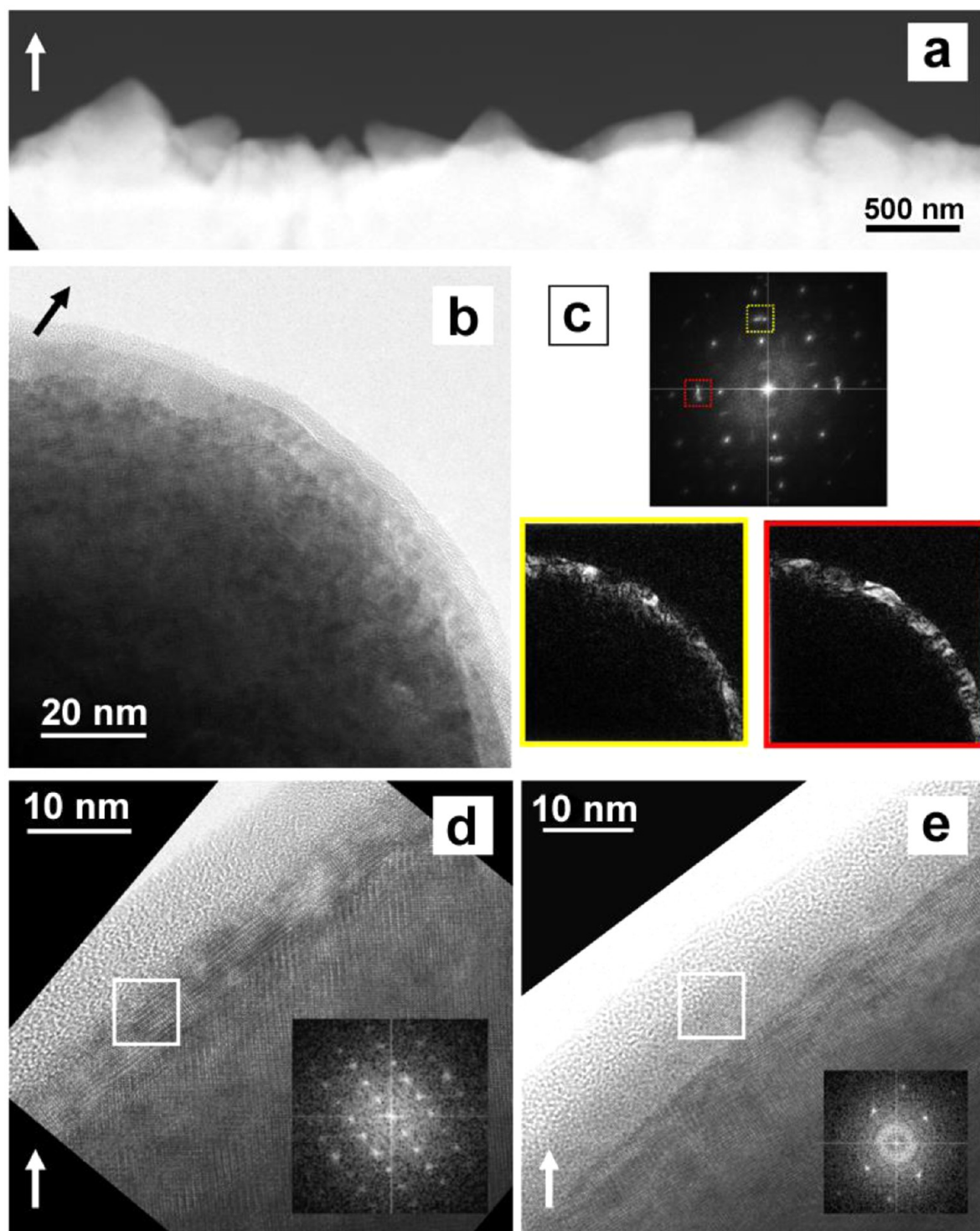


**Figure 5.** Cross-sectional (a) HAADF-STEM micrograph and (b, d, e) HR-TEM images of the  $\alpha$ -Fe<sub>2</sub>O<sub>3</sub>–Ti sample. Arrows indicate the growth direction. Image (c) refers to the top of the FFT image in (b), which shows spots related to  $\alpha$ -Fe<sub>2</sub>O<sub>3</sub> in  $\langle -4, -2, 1 \rangle$  zone axis and extra-spots (corresponding to a lattice distance of  $\approx 0.25$  nm) related to the surface overlayer. The yellow and red rectangles mark the areas selected for inverse FFT analysis. Images obtained from the yellow and red selections are reported in (c), bottom left and right, respectively. The insets in (d) and (e) are the FFTs of the areas marked by white squares in the corresponding HR-TEM images. They can be indexed to titanomagnetite in  $\langle 1, 1, 2 \rangle$  and  $\langle 1, 5, 2 \rangle$  zone axes, respectively.

in  $\alpha$ -Fe<sub>2</sub>O<sub>3</sub> and  $\epsilon$ -Fe<sub>2</sub>O<sub>3</sub>.<sup>38</sup> Ti2p peaks closely resembled those reported for titanium(IV) in an oxide environment.<sup>13,39</sup> Furthermore, the Fe2p/Ti2p intensity ratio ( $\approx 1.7$  for both specimens) indicated that the ALD process resulted in a comparable surface composition and a similar surface coverage of Fe<sub>2</sub>O<sub>3</sub> deposits.

In order to perform a detailed characterization of the ALD surface layer, TEM investigation was undertaken. Cross-sectional images of the  $\alpha$ -Fe<sub>2</sub>O<sub>3</sub>–Ti sample displayed regularly shaped grains (Figure 5a), conformally covered by a thin crystalline layer ( $< 10$  nm, Figure 5b). The FFT analysis showed regular spots belonging to the  $\alpha$ -Fe<sub>2</sub>O<sub>3</sub> phase, along with the occurrence of

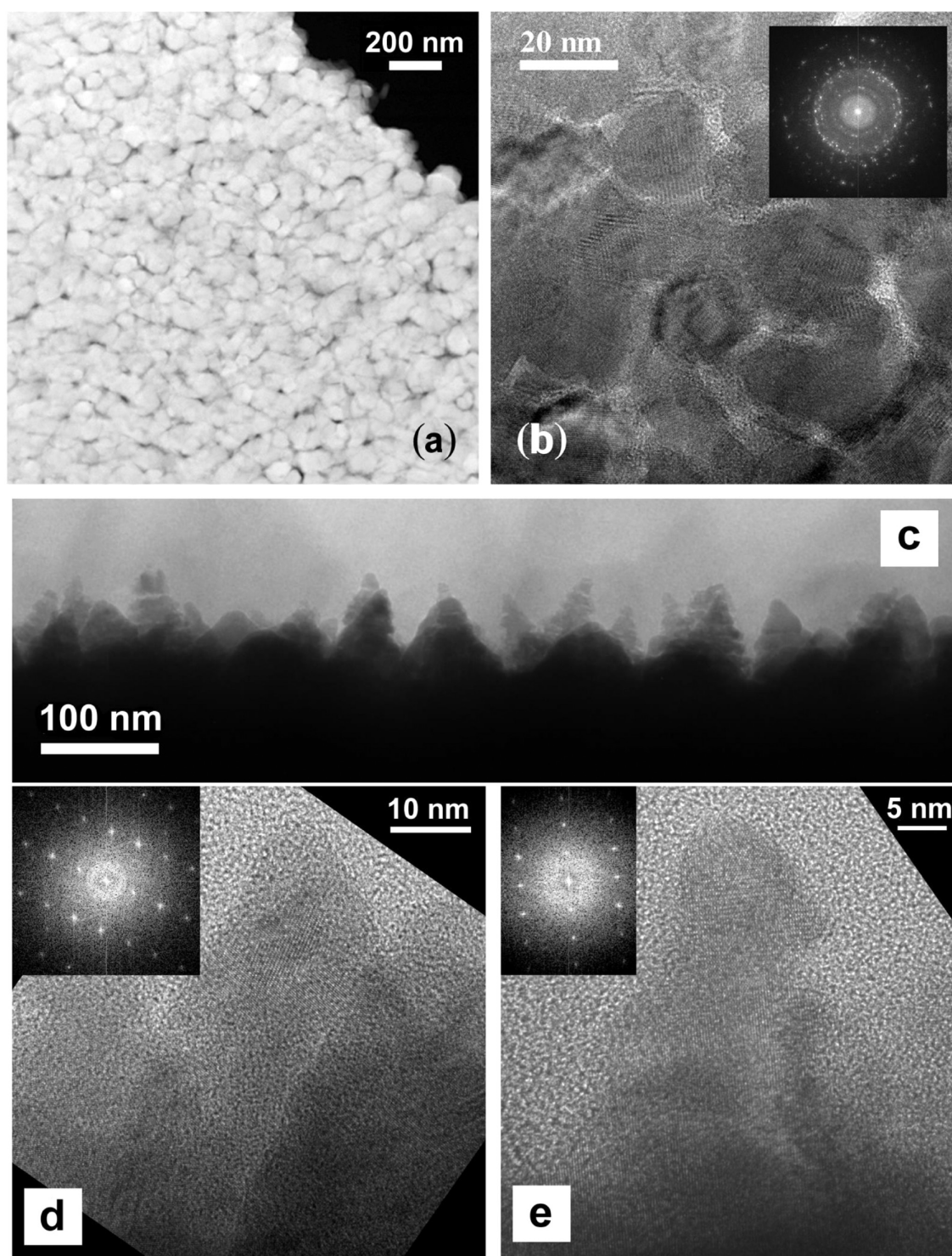


**Figure 6.** Plane-view (a) HAADF-STEM and (b) HR-TEM images of  $\epsilon$ -Fe<sub>2</sub>O<sub>3</sub>-Ti. The inset in (b) is the FFT of the HR-TEM micrograph. Cross-sectional (c) HAADF-STEM image and (d, e) HR-TEM images of  $\epsilon$ -Fe<sub>2</sub>O<sub>3</sub>-Ti. The insets in (d) and (e) are the FFTs of the HR-TEM images, which can be indexed to titanomagnetite in  $\langle 0,1,3 \rangle$  and  $\langle 1,1,2 \rangle$  zone axis, respectively.

diffused extra-spots (see Figure 5c, enclosed in red and yellow rectangles) related to the copresence of a different crystalline lattice. When a mask was applied to the FFT around one of these extraspots, the inverse FFT (left and right bottom images in Figure 5c) selectively showed the outermost layer structure. For the latter, HR-TEM analysis evidenced a mosaic texture, with subregions characterized by a well-defined orientation and lattice structure (Figures 5d, e).

Such a structure could not be related either to  $\alpha$ -Fe<sub>2</sub>O<sub>3</sub> or to TiO<sub>2</sub>, in any of the rutile, brookite, and anatase polymorphs. This finding suggested that the iron oxide matrix underwent a solid state reaction during the ALD process, resulting in the ultimate formation of a surface Fe-Ti-O overlayer. To this aim, the comparison of experimental FFTs with various ternary structure projections evidenced the occurrence of a cubic inverse spinel Fe<sub>3-x</sub>Ti<sub>x</sub>O<sub>4</sub> phase (titanomagnetite).<sup>40</sup> The Ti content in this phase



could not be accurately quantified neither from structural measurements, because of the very small variations in lattice parameter with  $x$  (<2% for  $x = 1$ ), nor from TEM energy-dispersive X-ray spectroscopy (EDXS), because of the very low signal-to-noise ratio.

Figure 6 displays the plane-view HAADF image (Figure 6a) and the HR-TEM micrograph (Figure 6b) of the  $\epsilon$ -Fe<sub>2</sub>O<sub>3</sub>-Ti sample. As in the case of the  $\alpha$ -Fe<sub>2</sub>O<sub>3</sub>-Ti specimen (see above), TEM-EDXS investigation of titanium presence was attempted, but the detected Ti signal was too weak to allow any spatial mapping. As a consequence, a deeper analysis was performed in cross-sectional geometry, investigating the phase composition of irregularly shaped structures formed on the surface of  $\epsilon$ -Fe<sub>2</sub>O<sub>3</sub> (Figure 6c). Similarly to the previous specimen, well-defined areas that could be indexed to the Fe<sub>3-x</sub>Ti<sub>x</sub>O<sub>4</sub> titanomagnetite phase along different projections (Figure 6d, e), could be detected in the outermost sample region. Taken together, these observations unequivocally confirmed that the ALD process responsible for the ternary phase formation was limited to the outermost sample layers for both  $\alpha$ - and  $\epsilon$ -Fe<sub>2</sub>O<sub>3</sub> specimens.

**Photoactivated Properties.** On the basis of the above results, particular attention was dedicated to the study of light-assisted properties of Fe-Ti-O materials, that have been scarcely investigated so far. To this regard, Figure 7 displays the

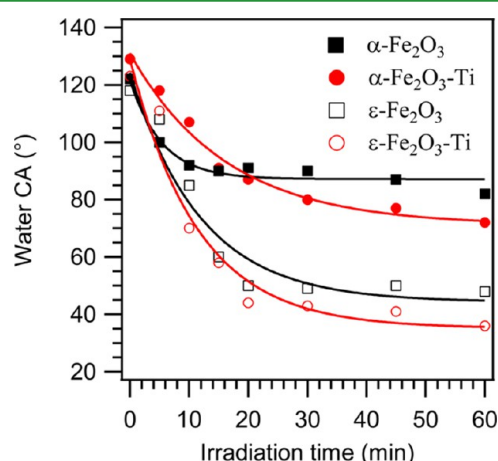


**Figure 7.** Water contact angle as a function of UV irradiation time for  $\alpha$ -Fe<sub>2</sub>O<sub>3</sub> or  $\epsilon$ -Fe<sub>2</sub>O<sub>3</sub> samples before and after ALD functionalization.

results of water CA measurements under UV irradiation. As can be observed, irrespective of the Fe<sub>2</sub>O<sub>3</sub> polymorph and ALD functionalization, the initial values were comprised between 120 and 130°. This phenomenon, indicating an hydrophobic state, can be traced back to the presence of aliphatic carbon species, because of air exposure, in the outermost sample layers.<sup>27,41</sup> Under UV irradiation (Figure 7), a progressive CA decrease was observed for all specimens, revealing the occurrence of a progressive hydrophobic-to-hydrophilic conversion as a function of time.

After 60 min, final water CA values were found to decrease in the order  $\alpha$ -Fe<sub>2</sub>O<sub>3</sub>  $\geq$   $\alpha$ -Fe<sub>2</sub>O<sub>3</sub>-Ti >  $\epsilon$ -Fe<sub>2</sub>O<sub>3</sub> >  $\epsilon$ -Fe<sub>2</sub>O<sub>3</sub>-Ti. Overall, these data suggest that  $\epsilon$ -Fe<sub>2</sub>O<sub>3</sub>-based specimens show an enhanced PH behavior with respect to the corresponding  $\alpha$ -Fe<sub>2</sub>O<sub>3</sub>-based ones. This effect is reasonably dependent on the different morphological organization of the iron oxide matrices,  $\epsilon$ -Fe<sub>2</sub>O<sub>3</sub> being characterized by a rodlike structure with a higher active area (see also PBD data in the Supporting Information section). An increase in the latter parameter likely results in a larger surface roughness and an higher amount of oxygen vacancies/hydroxyl groups, responsible for the enhanced

wettability observed upon irradiation.<sup>27,41–43</sup> Additional contributing phenomena are related to the different band gap and lifetime values of photogenerated charge carriers. Interestingly, ALD functionalization results in an improved hydrophilic behavior, an effect attributable to an increased charge separation at the Fe<sub>3-x</sub>Ti<sub>x</sub>O<sub>4</sub>/Fe<sub>2</sub>O<sub>3</sub> interface, as further described below.

The self-cleaning properties of the synthesized samples were evaluated by testing the PC oxidation of TPA to HTPA under UV irradiation by assuming zero-order and pseudo-first-order processes for HTPA formation and degradation, with rate constants  $k_1$  and  $k_2$ , respectively. Hence, the time dependence of HTPA concentration could be described on the basis of eqs 1 and 2:<sup>32</sup>

$$\frac{d[\text{HTPA}]}{dt} = k_1 - k_2[\text{HTPA}] \quad (1)$$

$$[\text{HTPA}] = \frac{k_1}{k_2}(1 - e^{-k_2 t}) \quad (2)$$

As an example, Figure 8 reports a representative [HTPA] vs. irradiation time curve for  $\alpha$ -Fe<sub>2</sub>O<sub>3</sub> specimen. Starting from similar

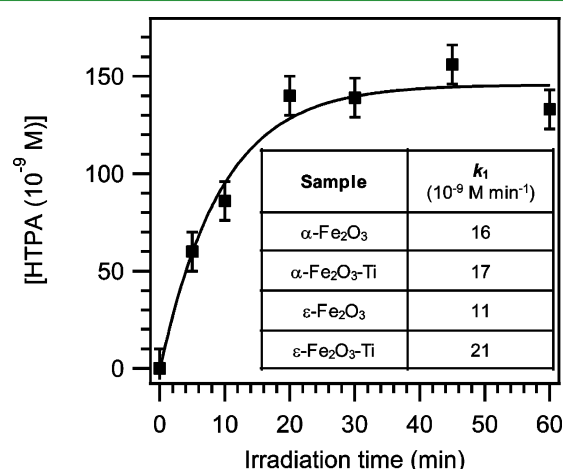


**Figure 8.** PC behavior of specimen  $\alpha$ -Fe<sub>2</sub>O<sub>3</sub>: HTPA concentration as a function of UV irradiation time. In the inset,  $k_1$  rate constant values are provided for  $\alpha$ - and  $\epsilon$ -Fe<sub>2</sub>O<sub>3</sub> samples before and after ALD functionalization.

data plots, the  $k_1$  values reported in the figure inset were obtained for each sample. In line with water CA measurements, these data evidenced improved PC performances for  $\epsilon$ -Fe<sub>2</sub>O<sub>3</sub> after ALD functionalization. Notably, the  $k_1$  rate constant obtained in the present work for the  $\epsilon$ -Fe<sub>2</sub>O<sub>3</sub>-Ti sample was higher than the value reported under the same conditions for ZnO nanorods<sup>41</sup> and commercial Pilkington Activ glass,<sup>32</sup> which showed  $k_1$  values of ca.  $9.5 \times 10^{-9}$  and  $2.1 \times 10^{-9}$  M min<sup>-1</sup>, respectively. Such results highlight the inherent technological potential of the present specimens for eventual self-cleaning applications. Overall,  $\epsilon$ -Fe<sub>2</sub>O<sub>3</sub>-Ti materials show attractive performances for both PH and PC applications.

In an attempt to gain a deeper insight into the observed CA and PC trends, PBD analyses (see the Supporting Information section) were performed, obtaining the band gap and carrier lifetime values collected in Table 1.

Compared to the bare iron oxide polymorphs, a slight increase of both  $E_g$  and  $\tau$  values took place after the ALD process. Such effects were traced back to the conformal coverage of the Fe<sub>2</sub>O<sub>3</sub> deposits by the Fe<sub>3-x</sub>Ti<sub>x</sub>O<sub>4</sub> phase. In particular, the intimate



**Table 1. Band Gap ( $E_g$ ) and Minority Carrier Lifetime ( $\tau$ ) Values Obtained from PBD Experiments**

sample	$E_g$ (eV)	$\tau$ (ps)
$\alpha$ -Fe <sub>2</sub> O <sub>3</sub>	2.2 ± 0.1	6.4 ± 0.3
$\alpha$ -Fe <sub>2</sub> O <sub>3</sub> -Ti	2.5 ± 0.2	10.6 ± 0.4
$\epsilon$ -Fe <sub>2</sub> O <sub>3</sub>	2.0 ± 0.2	7.2 ± 0.3
$\epsilon$ -Fe <sub>2</sub> O <sub>3</sub> -Ti	2.2 ± 0.2	11.8 ± 0.4

Fe<sub>2</sub>O<sub>3</sub>/Fe<sub>3-x</sub>Ti<sub>x</sub>O<sub>4</sub> interfacial contact likely resulted in an improved charge carrier separation and passivation of iron oxide surface trap states.<sup>6,14,22</sup> As a consequence, both PH and PC performances are enhanced upon titanomagnetite deposition.

## CONCLUSIONS

The present work has introduced a joint ALD/CVD synthetic strategy to develop a tailored surface functionalization of supported Fe<sub>2</sub>O<sub>3</sub> nanosystems. This goal is readily fulfilled by the selective CVD deposition of  $\alpha$ -Fe<sub>2</sub>O<sub>3</sub> or  $\epsilon$ -Fe<sub>2</sub>O<sub>3</sub> under suitably optimized conditions, followed by ALD using Ti(OPr)<sub>4</sub> and water as precursors. A thorough material characterization revealed the formation of an ultrathin titanomagnetite (Fe<sub>3-x</sub>Ti<sub>x</sub>O<sub>4</sub>) layer uniformly covering the underlying iron oxide deposits. The reported results highlight that the optimization of Fe<sub>2</sub>O<sub>3</sub>/Fe<sub>3-x</sub>Ti<sub>x</sub>O<sub>4</sub> interfacial interactions was the key tool to develop efficient materials for light-assisted (e.g., antifogging, self-cleaning) applications, as demonstrated by PH and PC properties. In this regard, the use of systems based on the scarcely studied  $\epsilon$ -Fe<sub>2</sub>O<sub>3</sub> polymorph enabled to achieve performances superior to those containing the most conventional  $\alpha$ -Fe<sub>2</sub>O<sub>3</sub> one.

As a whole, this work demonstrates the possibility to obtain smart nanomaterials through an advanced engineering of their surface properties. It is reasonable that the above interfacial phenomena could beneficially affect functional performances also in other related technological applications, such as photovoltaics and light-emitting diodes. To this aim, the extension of the proposed approach to other oxide heteronanostructures with controlled composition, structure, and morphology is currently under investigation in our laboratories.

## ASSOCIATED CONTENT

### Supporting Information

FE-SEM micrographs of  $\alpha$ -Fe<sub>2</sub>O<sub>3</sub> and  $\epsilon$ -Fe<sub>2</sub>O<sub>3</sub>, a description of the PBD technique, as well as morphological surface parameters obtained from PBD analyses of the bare iron oxide specimens. This material is available free of charge via the Internet at <http://pubs.acs.org>.

## AUTHOR INFORMATION

### Corresponding Author

\*E-mail: chiara.maccato@unipd.it.

### Notes

The authors declare no competing financial interest.

## ACKNOWLEDGMENTS

The authors kindly acknowledge the financial support under the FP7 project SOLAROGENIX (NMP4-SL-2012-310333), as well as from Padova University ex-60% 2012 (60A03-5517), PRAT 2010 (CPDA102579) and Regione Lombardia-INSTM AT-LANTE projects. V. Grillo (CNR-Nano) is acknowledged for helpful discussions about TEM analysis. G. Beuckert and I. Paloumpa (BTU-Cottbus) and the Bessy-II staff (HZB) are also

acknowledged for the technical support during the ALD deposition and the XPS measurements, respectively. Nova Gorica University gratefully acknowledges financial support from the SUNGREEN project (FP7-REGPOT-2011-1).

## REFERENCES

- (1) Carraro, G.; Barreca, D.; Maccato, C.; Bontempi, E.; Depero, L. E.; de Julian Fernandez, C.; Caneschi, A. *CrystEngComm* **2013**, *15*, 1039–1042.
- (2) Sivula, K.; Le Formal, F.; Grätzel, M. *ChemSusChem* **2011**, *4*, 432–449.
- (3) Dotan, H.; Kfir, O.; Sharlin, E.; Blank, O.; Gross, M.; Dumchin, I.; Ankonina, G.; Rothschild, A. *Nat. Mater.* **2013**, *12*, 158–164.
- (4) Alexander, B. D.; Kulesza, P. J.; Rutkowska, I.; Solarska, R.; Augustynski, J. *J. Mater. Chem.* **2008**, *18*, 2298–2303.
- (5) Katz, M. J.; Riha, S. C.; Jeong, N. C.; Martinson, A. B. F.; Farha, O. K.; Hupp, J. T. *Coord. Chem. Rev.* **2012**, *256*, 2521–2529.
- (6) Le Formal, F.; Tetreault, N.; Cornuz, M.; Moehl, T.; Grätzel, M.; Sivula, K. *Chem. Sci.* **2011**, *2*, 737–743.
- (7) Singh, A. P.; Mettenbörger, A.; Golus, P.; Mathur, S. *Int. J. Hydrogen Energy* **2012**, *37*, 13983–13988.
- (8) Agarwala, S.; Lim, Z. H.; Nicholson, E.; Ho, G. W. *Nanoscale* **2012**, *4*, 194–205.
- (9) Hamann, T. W. *Dalton Trans.* **2012**, *41*, 7830–7834.
- (10) Thimsen, E.; Le Formal, F.; Grätzel, M.; Warren, S. C. *Nano Lett.* **2010**, *11*, 35–43.
- (11) Vincent, T.; Gross, M.; Dotan, H.; Rothschild, A. *Int. J. Hydrogen Energy* **2012**, *37*, 8102–8109.
- (12) Hahn, N. T.; Ye, H.; Flaherty, D. W.; Bard, A. J.; Mullins, C. B. *ACS Nano* **2010**, *4*, 1977–1986.
- (13) Mor, G. K.; Prakasam, H. E.; Varghese, O. K.; Shankar, K.; Grimes, C. A. *Nano Lett.* **2007**, *7*, 2356–2364.
- (14) Mayer, M. T.; Lin, Y.; Yuan, G.; Wang, D. *Acc. Chem. Res.* **2013**, DOI: 10.1021/ar300302z.
- (15) Kronawitter, C. X.; Bakke, J. R.; Wheeler, D. A.; Wang, W.-C.; Chang, C.; Antoun, B. R.; Zhang, J. Z.; Guo, J.; Bent, S. F.; Mao, S. S.; Vayssieres, L. *Nano Lett.* **2011**, *11*, 3855–3861.
- (16) Paracchino, A.; Laporte, V.; Sivula, K.; Grätzel, M.; Thimsen, E. *Nat. Mater.* **2011**, *10*, 456–461.
- (17) Li, T. C.; Góes, M. r. S.; Fabregat-Santiago, F.; Bisquert, J.; Bueno, P. R.; Prasittichai, C.; Hupp, J. T.; Marks, T. J. *J. Phys. Chem. C* **2009**, *113*, 18385–18390.
- (18) Im, J. S.; Lee, S. K.; Lee, Y.-S. *Appl. Surf. Sci.* **2011**, *257*, 2164–2169.
- (19) Leskelä, M.; Ritala, M. *Thin Solid Films* **2002**, *409*, 138–146.
- (20) Leskelä, M.; Ritala, M. *Angew. Chem., Int. Ed.* **2003**, *42*, 5548–5554.
- (21) Kim, H.; Lee, H.-B.-R.; Maeng, W. J. *Thin Solid Films* **2009**, *517*, 2563–2580.
- (22) Kobylinska, D. K.; Bukowski, R. J.; Burak, B.; Bodzenta, J.; Kochowski, S. *J. Appl. Phys.* **2006**, *100*, 063501-1–063501-9.
- (23) Rezlescu, E.; Doroftei, C.; Rezlescu, N.; Popa, P. D. *Phys. Status Solidi A* **2008**, *205*, 1790–1793.
- (24) Tan, O. K.; Cao, W.; Zhu, W.; Chai, J. W.; Pan, J. S. *Sens. Actuators, B* **2003**, *93*, 396–401.
- (25) Barreca, D.; Carraro, G.; Devi, A.; Fois, E.; Gasparotto, A.; Seraglia, R.; Maccato, C.; Sada, C.; Tabacchi, G.; Tondello, E.; Venzo, A.; Winter, M. *Dalton Trans.* **2012**, *41*, 149–155.
- (26) Gasparotto, A.; Carraro, G.; Barreca, D.; Maccato, C.; Tondello, E. patent PCT/IT2012/000276, 2012.
- (27) Barreca, D.; Gasparotto, A.; Maccato, C.; Tondello, E.; Lavrenčič Štangar, U.; Patil, S. R. *Surf. Coat. Technol.* **2009**, *203*, 2041–2045.
- (28) Barreca, D.; Carraro, G.; Gasparotto, A.; Maccato, C.; Seraglia, R.; Tabacchi, G. *Inorg. Chim. Acta* **2012**, *380*, 161–166.
- (29) Barreca, D.; Gasparotto, A.; Maccato, C.; Tondello, E.; Lebedev, O. I.; Van Tendeloo, G. *Cryst. Growth Des.* **2009**, *9*, 2470–2480.
- (30) Tallarida, M.; Weisheit, M.; Kolanek, K.; Michling, M.; Engelmann, H. J.; Schmeisser, D. *J. Nanopart. Res.* **2011**, *13*, S975–S983.

- (31) Tallarida, M.; Schmeisser, D. *Semicond. Sci. Technol.* **2012**, *27*, 074010-1–074010-9.
- (32) Černigoj, U.; Kete, M.; Lavrenčič Štangar, U. L. *Catal. Today* **2010**, *151*, 46–52.
- (33) *Joint Committee on Powder Diffraction Standards Pattern No. 33–0664*; International Centre for Diffraction Data: Newtown Square, PA, 2000.
- (34) *Inorganic Crystal Structure Database Pattern No. 51122*; FIZ Karlsruhe: Karlsruhe, Germany, 2007.
- (35) Tartaj, P.; Morales, M. P.; Gonzalez-Carreño, T.; Veintemillas-Verdaguer, S.; Serna, C. J. *Adv. Mater.* **2011**, *23*, 5243–5249.
- (36) Fujii, T.; de Groot, F. M. F.; Sawatzky, G. A.; Voogt, F. C.; Hibma, T.; Okada, K. *Phys. Rev. B* **1999**, *59*, 3195–3202.
- (37) Droubay, T.; Chambers, S. A. *Phys. Rev. B* **2001**, *64*, 205414-1–205414-6.
- (38) Grosvenor, A. P.; Kobe, B. A.; Biesinger, M. C.; McIntyre, N. S. *Surf. Interface Anal.* **2004**, *36*, 1564–1574.
- (39) Diebold, U. *Surf. Sci. Rep.* **2003**, *48*, 53–229.
- (40) Bosi, F.; Halenius, U.; Skogby, H. *Am. Mineral.* **2009**, *94*, 181–189.
- (41) Bekermann, D.; Gasparotto, A.; Barreca, D.; Devi, A.; Fischer, R. A.; Kete, M.; Lavrenčič Štangar, U.; Lebedev, O. I.; Maccato, C.; Tondello, E.; Van Tendeloo, G. *ChemPhysChem* **2010**, *11*, 2337–2340.
- (42) Papadopoulou, E. L.; Barberoglou, M.; Zorba, V.; Manousaki, A.; Pagkozidis, A.; Stratakis, E.; Fotakis, C. *J. Phys. Chem. C* **2009**, *113*, 2891–2895.
- (43) Zhang, L.; Dillert, R.; Bahnemann, D.; Vormoor, M. *Energy Environ. Sci.* **2012**, *5*, 7491–7507.